

# *SpatialCrafter*: Unleashing the Imagination of Video Diffusion Models for Scene Reconstruction from Limited Observations

Songchun Zhang<sup>1</sup> Huiyao Xu<sup>1</sup> Sitong Guo<sup>1</sup> Zhongwei Xie<sup>3</sup> Pengwei Liu<sup>1</sup>  
 Hujun Bao<sup>1</sup> Weiwei Xu<sup>1</sup> Changqing Zou<sup>1,2</sup>  
<sup>1</sup>Zhejiang University <sup>2</sup>Zhejiang Lab <sup>3</sup>Wuhan University

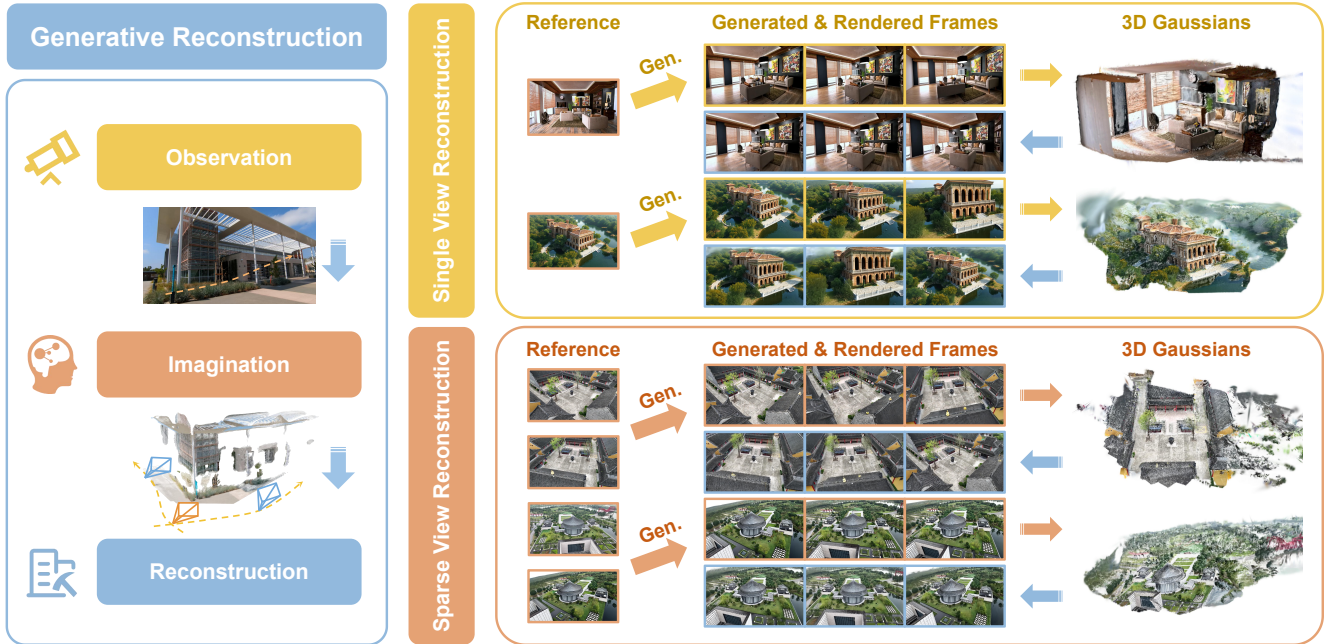


Figure 1. **Overview.** Our method, *SpatialCrafter*, generates additional novel views of a scene from few inputs by leveraging camera trajectory-guided video diffusion models, which alleviates the ambiguity of sparse view reconstruction and robustly reconstructs the scene from the generated video frames. It demonstrates impressive performance in both indoor and outdoor scenes, while also exhibiting generalization capabilities in real scenes and synthetic images. More visualization results can be found in the supplementary material.

## Abstract

*Novel view synthesis (NVS) boosts immersive experiences in computer vision and graphics. Existing techniques, though progressed, rely on dense multi-view observations, restricting their application. This work takes on the challenge of reconstructing photorealistic 3D scenes from sparse or single-view inputs. We introduce SpatialCrafter, a framework that leverages the rich knowledge in video diffusion models to generate plausible additional observations, thereby alleviating reconstruction ambiguity. Through a trainable camera encoder and an epipolar attention mechanism for explicit geometric constraints, we achieve precise camera control and 3D consistency, further reinforced by a*

*unified scale estimation strategy to handle scale discrepancies across datasets. Furthermore, by integrating monocular depth priors with semantic features in the video latent space, our framework directly regresses 3D Gaussian primitives and efficiently processes long-sequence features using a hybrid network structure. Extensive experiments show our method enhances sparse view reconstruction and restores the realistic appearance of 3D scenes.*

## 1. Introduction

Novel View Synthesis (NVS), as a key technology in computer vision and graphics, provides crucial support for immersive experiences in fields such as video games and

mixed reality. Although neural reconstruction techniques have made significant progress in recent years [25, 38, 41, 58, 62], these methods typically rely on dense multi-view observation data, which face numerous limitations in practical applications. Therefore, this paper focuses on a more practically valuable challenge: how to achieve high-quality 3D scene reconstruction and synthesize realistic novel views from sparse or even single-view observation.

The complexity of this problem stems from three main aspects: first, the diversity and complexity of real-world scene make precise modeling extremely challenging; second, occluded regions in sparse viewpoints are difficult to recover; and finally, limited geometric cues constrain the accuracy of reconstruction. Compared to traditional methods that depend on numerous viewpoints, achieving high-quality reconstruction from sparse views requires stronger prior knowledge and more efficient reasoning capabilities, which is the core challenge of this problem. To address these challenges, some methods [18, 26, 29, 39, 77, 81] constrain the optimization process by introducing regularization terms, but these methods need to be optimized for each scene, are not generalizable, and are difficult to cope with complex scenarios. Recently, some feed-forward methods [8, 9, 22, 48, 53, 56, 73, 74] have achieved generalizable sparse view scene reconstruction by directly predicting 3D Gaussian primitives for each pixel. However, such methods produce severe artifacts and implausible images when reconstructing occluded regions and applying them to the extrapolation setting. To address this challenge, some methods [34, 43, 60, 61] have introduced the priors from the diffusion model to achieve sparse or single-view NVS, but they perform poorly on scene-level data and lack precise pose control and 3D consistency. This is due to the fact that low-dimensional camera information such as Euler angles and extrinsic struggle to provide comprehensive control signals to the generative models.

In this paper, we propose a framework named *Spatial-Crafter* for scene reconstruction and novel view synthesis based on sparse or single-view inputs. Our innovation lies in leveraging the rich physical world knowledge embedded in video diffusion models to provide plausible additional observations for scene reconstruction, thereby effectively reducing the problem complexity. Specifically, we first focus on enhancing precise camera control and 3D consistency in generated videos. To achieve this, we parameterize camera settings using ray embeddings or metric depth-warped images and incorporate them into the video diffusion model via a trainable camera encoder. Furthermore, we propose an epipolar attention mechanism that improves 3D consistency between video frames through explicit geometric constraints. Previous methods [20, 60] often experience performance degradation and difficulty generating large-motion videos when trained on multiple scene

datasets. We identified that these issues primarily stem from scale ambiguity in scene datasets. To overcome this, we introduce a unified scale estimator to calibrate scene dataset, enabling effective joint training across multiple datasets.

Although we can generate visually coherent video sequences, relying solely on generated frames to reconstruct general scenes often leads to suboptimal solutions, particularly in large-scale outdoor environments and stylized scenes. To address this, we propose incorporating monocular depth priors with rich semantic features extracted from the video latent space. Leveraging these latent features, our method directly regresses 3D Gaussian primitives of the scene via a feed-forward network. Furthermore, to efficiently handle long-sequence feature interactions, we design a hybrid architecture that integrates Mamba blocks with Transformer blocks. Experiments show that our method not only improves the sparse-view reconstruction, but also accurately restores the appearance of 3D scenes, especially when extrapolating from a single view and when there are few sparse view overlaps. In conclusion, our key contributions can be summarized as follows:

- We introduce a framework that effectively utilizes the physical-world knowledge embedded in video diffusion models to provide additional plausible observations for sparse-view scene reconstruction, thus reducing the ambiguity of sparse view scene reconstruction.
- To address the scale ambiguity problem that occurs in joint training across datasets, we develop a unified scale estimation approach for trajectory calibration. This solves the performance degradation problem, thus enabling effective multi-dataset training.
- We combine monocular depth priors with semantic features extracted from the video latent space, and directly regress 3D Gaussian primitives through a feed-forward manner. Meanwhile, we propose a hybrid architecture integrating Mamba blocks with Transformer blocks to efficiently handle long-sequence feature interactions.

## 2. Related Work

### 2.1. Sparse-View Scene Reconstruction

NeRF [58] and Gaussian Splatting [25] have achieved photorealistic representations of 3D scenes, but require optimization on densely collected image sets for each scene. To address this problem, some approaches [18, 29, 67, 81] focus on constraining the optimization process of 3D representations via manually designed regularization. Some other methods [8, 9, 23, 52, 65, 68] are trained on large-scale datasets and directly predict the 3D representation in a feed-forward manner. Recently, some approaches [14, 30, 33, 48] based on end-to-end 3D reconstruction models [28, 56], have achieved efficient and high-quality 3D reconstruction. However, these methods cannot handle oc-

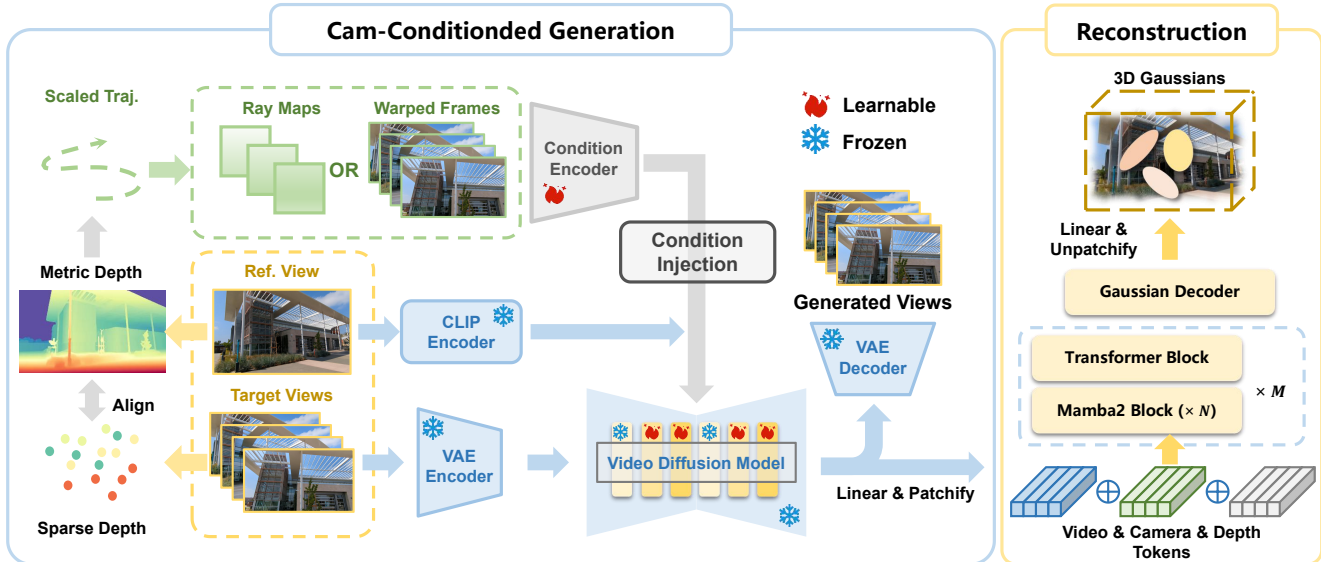


Figure 2. **Overview of our pipeline.** Our generative reconstruction pipeline consists of two parts: camera-controlled video generation, and then reconstruction. First, we set the exploration path based on the input views. In the video generation module, ray embedding is used to parameterize the camera information, and a cross-attention mechanism with epipolar constraints is introduced to improve the 3D consistency of the generated video. The robust 3D scene reconstruction pipeline integrates monocular depth priors with semantic features extracted from the video latent space, and directly regress 3D Gaussian primitives through a feed-forward manner.

cluded areas, and when reconstruction fails (*e.g.*, in the case of large viewpoint changes), the results of subsequent novel view synthesis can be significantly compromised.

## 2.2. Diffusion-based Novel View Synthesis

Since text-to-image diffusion models [42] contain rich natural image priors, some methods [40, 59] directly optimize 3D representations [25, 58] via score distillation sampling [40]. Several approaches [7, 34, 43, 54] enable zero-shot novel view synthesis by fine-tuning the image and pose-conditioned generative models on large-scale 3D object [11] or scene [54, 80] datasets. However, they still have difficulty synthesizing consistent novel views. To solve this, some approaches [6, 16, 35, 37, 45, 61, 78] generate multi-views simultaneously and model the correlation between multiple views with ground-truth poses. Some recent methods [30, 36] proposed to use large-scale unposed images to train NVS methods. In addition, some methods [10, 13, 15, 46, 70, 76] utilize depth-based warping to synthesize novel views and employ the T2I model to inpaint the warped images. However, the novel views generated by these methods tend to suffer from artifacts and cumulative errors, limiting their use in generalized scenes.

## 2.3. Controllable Video Generation

While recent text-to-video diffusion models have achieved remarkable progress, they inherit the controllability limitations of their text-to-image counterparts, often requir-

ing additional conditioning mechanisms to align generated videos with user intent. Several works [19, 24, 57, 66] have been carried out to introduce a variety of conditions into video generation models. Recently, attention has focused on controlling the camera motion of the video. Some approaches [19, 51] employ motion-specific training for predefined camera movements, though this framework struggles with complex trajectory synthesis. Some methods [20, 60, 63] enable more complex camera control by parameterizing the camera trajectory and injecting it into a pre-trained video diffusion model via a trainable camera encoder. MotionCtrl [60] controls camera and object motions independently through learnable adapters, while CameraCtrl [20] introduces Plücker embeddings for accurate 6-DoF camera pose representation. AC3D [1] optimizes the pose adjustment scheme to accelerate convergence and limits the injection of camera features to specific locations. ViewCrafter [71] and ReconX [33] pushes this direction by enabling pixel-accurate view compositing through point-based rendering formulation.

## 3. Method

This section begins by explaining our camera-controlled video generation model (Section 3.1), which employs ray embeddings for precise pose control. Then, we describe how to use epipolar geometry constraints to enhance 3D consistency in the video frames. Next, we introduce our scene reconstruction pipeline (Section 3.2), which aims

to perform stable 3D reconstruction based on the generated video latents. These innovations collectively improve the accuracy and consistency of 3D reconstructions from generated video.

### 3.1. Camera-Conditioned Video Generation

**Scale Alignment.** While recent methods [20, 60] have achieved promising results in novel view synthesis, their reliance on ground-truth camera extrinsic from Re10K [79] during inference inherently limits their applicability to in-the-wild scenarios. Moreover, the metric-scaled poses in Re10K create alignment challenges when jointly training with other datasets (e.g., DL3DV [31]) where poses are estimated using COLMAP, primarily due to scale ambiguity issues. To address this issue, we introduced a metric depth estimation model [5] to achieve scale alignment of camera poses between different datasets. During the data preprocessing stage, we align the metric 3D point cloud predicted by the model with the sparse point cloud generated using COLMAP to calculate the scale factor, thereby obtaining absolute-scale camera extrinsics.

**Camera Injection.** Inspired by recent methods [20, 47, 72], we chose to use ray embeddings [20] or the depth warping frames [71] to represent the camera information. This over-parameterized approach [72] provides more accurate pose information to the video generator than other methods. Specifically, for a ray defined by the origin  $o \in \mathbb{R}^3$  and the normalized direction  $d \in \mathbb{R}^3$ , we can represent it as  $(o \times d, d) \in \mathbb{R}^6$ . Given the camera parameters, the direction of the ray  $d'$  corresponding to the pixel coordinates  $(u, v)$  can be calculated as  $d' = \mathbf{R}\mathbf{K}^{-1}(u, v, 1)^\top + \mathbf{T}$ . For depth warping frames, we leverage the pretrained depth estimation model [55] to map the reference image into a 3D point cloud. Subsequently, we render novel views at specified camera poses by projecting this point cloud via the target camera parameters. Afterwards, we use a trainable conditional encoder to inject the camera information into the video model instead of fine-tuning all model parameters. The training objective is:

$$\mathcal{L} = \mathbb{E}_{z, z_0, \epsilon, \mathbf{P}, t} \left[ \|\epsilon - \epsilon_\theta(z_t; z_0, t, \phi(c))\|_2^2 \right] \quad (1)$$

where  $\mathbf{P}$  represents the ray embeddings,  $z_0$  denotes the latent embeddings of the reference frame, and  $t$  indicates the timestamps.

**Epipolar Feature Aggregation.** Camera embedding enhances control but 3D video consistency remains challenging due to dense self-attention allowing unrestricted cross-frame pixel interactions. We address this by incorporating epipolar geometric constraints, and aggregating features along epipolar lines. For a pixel  $\mathbf{p} = (u, v)$  in frame  $i$ , its corresponding epipolar line  $l_{ik}$  in frame  $k$  is computed as  $l_{ik}(\mathbf{p}) = \mathbf{F}_{ik} \cdot \tilde{\mathbf{p}}$ , where  $\tilde{\mathbf{p}} = (u, v, 1)^\top$  are the ho-

mogeneous coordinates, and  $\mathbf{F}_{ik} \in \mathbb{R}^{3 \times 3}$  is the fundamental matrix. The fundamental matrix is decomposed as  $\mathbf{F}_{ik} = \mathbf{K}_k^{-\top} \mathbf{E}_{ik} \mathbf{K}_i^{-1}$ , where  $\mathbf{K}_i, \mathbf{K}_k \in \mathbb{R}^{3 \times 3}$  are the camera intrinsics, and  $\mathbf{E}_{ik}$  is the essential matrix. We then convert epipolar lines into attention masks by computing per-pixel distances and applying a threshold, restricting attention to geometrically valid regions.

**Sparse-View Setting.** To adapt to the sparse view input setting, we formulate the task as a video frame interpolation problem conditioned on the given start and end frames. To maximally preserve the priors from the pre-trained models [4], we inject boundary frame conditions in both latent and semantic space. Specifically, we combine latent features of the first and last frames with their noisy latent representations, and then concatenate the extracted CLIP embeddings from both frames for cross-attentional feature injection. The training objective is:

$$\mathcal{L} = \mathbb{E}_{z, z_0, z_n, \epsilon, \mathbf{P}, t} \left[ \|\epsilon - \epsilon_\theta(z_t; z_0, z_n, t, \mathbf{P})\|_2^2 \right] \quad (2)$$

where  $z_n$  and  $z_0$  are the latent embeddings of the final and initial frames, respectively. During the inference phase, we use DUST3R to estimate the extrinsic and intrinsic parameters for the input views.

### 3.2. Video-based Scene Reconstruction

**Motivation.** There are several challenges in reconstructing scenes directly from generated videos. First, the limited number of generated frames makes it difficult to capture complete scene information. In addition, the diverse styles of video frames can pose a challenge to traditional reconstruction techniques. Furthermore, the generated video frames may contain imperfect or low-quality areas, making the reconstruction process unstable. Moreover, In stylized scenes, previous methods often yield poor results, as recovering poses and sparse point clouds from video frames is difficult, leading to many artifacts. To address this, a powerful reconstruction module specifically designed to handle the generated videos is required.

**Latent Feature Fusion.** Given input video latents  $\mathbf{z} \in \mathbb{R}^{T \times H \times W \times C}$  and camera poses encoded as ray embeddings  $\mathbf{p} \in \mathbb{R}^{T \times H \times W \times 6}$ , we transform them into token sequences through a patchification process. Specifically, we apply spatial patchification to latent features to obtain latent tokens  $\mathbf{z}_t \in \mathbb{R}^{N \times d_z}$ , while ray embeddings undergo 3D-patchification to produce pose tokens  $\mathbf{p}_t \in \mathbb{R}^{N \times d_p}$ . To incorporate explicit geometric guidance, we leverage monocular depth estimation within our pipeline. For each input RGB video frame, we estimate dense depth maps  $\mathbf{D} \in \mathbb{R}^{T \times H \times W \times 1}$ , which are processed by a dedicated depth encoder to yield depth tokens  $\mathbf{d}_t \in \mathbb{R}^{N \times d_d}$ . The three token sets are channel-wise concatenated to form a unified representation  $\mathbf{x} = [\mathbf{z}_t; \mathbf{p}_t; \mathbf{d}_t] \in \mathbb{R}^{N \times (d_z + d_p + d_d)}$ ,



Figure 3. **Qualitative comparison of generated videos.** Compared to other benchmark methods, the videos generated by our method have better foreground object-background consistency, while also being able to generate videos with larger motion amplitude.

Method	FVD↓	FID↓	R <sub>err</sub> ↓	T <sub>err</sub> ↓	LPIPS↓	PSNR↑	SSIM↑
<b>RealEstate10K</b>							
MotionCtrl [60]	22.65	230.12	0.234	0.798	0.299	14.72	0.404
CameraCtrl [20]	21.48	188.21	0.054	0.127	0.230	17.33	0.516
ViewCrafter [71]	20.96	204.18	0.055	0.153	0.215	18.95	0.503
Ours	<b>18.25</b>	<b>183.25</b>	<b>0.052</b>	<b>0.103</b>	<b>0.207</b>	<b>19.21</b>	<b>0.523</b>
<b>Tanks-and-Temples</b>							
MotionCtrl [60]	30.25	290.38	0.838	1.505	0.315	14.64	0.388
CameraCtrl [20]	24.41	244.82	0.118	0.294	0.285	15.38	0.469
ViewCrafter [71]	22.50	231.35	0.126	0.307	0.247	<b>16.24</b>	<b>0.508</b>
Ours	<b>20.17</b>	<b>192.52</b>	<b>0.097</b>	<b>0.175</b>	<b>0.228</b>	16.12	0.501
<b>DL3DV</b>							
MotionCtrl [60]	25.65	249.51	0.473	1.118	0.312	14.38	0.386
CameraCtrl [20]	22.76	233.54	0.095	0.238	0.262	16.33	0.489
ViewCrafter [71]	20.59	211.24	0.093	0.244	0.242	<b>17.12</b>	0.521
Ours	<b>18.21</b>	<b>171.52</b>	<b>0.063</b>	<b>0.134</b>	<b>0.225</b>	17.02	<b>0.537</b>

Table 1. **Quantitative comparison** to the camera conditioned video generation method on RealEstate10K, DL3DV, and Tanks-and-Temples dataset.

which is then linearly projected to a lower-dimensional space  $\mathbf{x}' \in \mathbb{R}^{N \times d}$  before being fed into a sequence of mamba and transformer blocks. Mamba [17] achieves the same token sequence processing functionality as Transformer, but reduces computational complexity from  $\mathcal{O}(L^2)$  to  $\mathcal{O}(L)$ , making it particularly suitable for dense reconstruction tasks. In our Mamba blocks, we implement bi-directional scanning across the token sequence. First, we compute state parameters  $\mathbf{A}, \mathbf{B}, \mathbf{C} \in \mathbb{R}^{N \times d}$  from the input tokens using a linear projection. Then, we execute the State Space Model (SSM) in both forward ( $\mathbf{y}_f$ ) and backward ( $\mathbf{y}_b$ ) directions. The final output of each Mamba block is computed as  $\mathbf{y} = \mathbf{y}_f + \mathbf{y}_b$  followed by a final linear transformation.

**Gaussian Decoding.** We design a lightweight decoder module that efficiently transforms output feature tokens into per-pixel Gaussian parameters. The decoding module consists of 3D-DeConv layers, which generates refined Gaussian feature map  $G \in \mathbb{R}^{(T \times H \times W) \times 12}$ . This 12-channel representation precisely encodes the complete set of Gaussian parameters: RGB color (3 channels), scale factors (3 channels), rotation quaternion (4 channels), opacity (1 channel),

and ray distance (1 channel). The final output of the model is the merge of 3D Gaussians from all input video frames.

**Training Objective.** During training, we render images from predicted Gaussians using randomly selected supervision views. Our approach employs a composite loss that integrates three components:

$$\mathcal{L}_{recon} = \lambda_1 \mathcal{L}_{mse} + \lambda_2 \mathcal{L}_{perc} + \lambda_3 \mathcal{L}_{depth}, \quad (3)$$

where  $\mathcal{L}_{mse}$  represents pixel-wise mean squared error,  $\mathcal{L}_{perc}$  denotes perceptual loss, and  $\mathcal{L}_{depth}$  enforces depth consistency. This formulation jointly optimizes for photometric accuracy, high-level perceptual fidelity, and geometric coherence.

## 4. Experiment

### 4.1. Experiment settings

**Datasets.** To comprehensively capture the underlying distribution of real-world scenarios, we trained our video diffusion model on three diverse datasets: RealEstate-10K [79], ACID [32], and DL3DV-10K [31]. The Re10K dataset from YouTube comprises 67,477 training and 7,289 testing indoor and outdoor camera trajectories. The ACID dataset focuses on natural landscapes, with 11,075 training and 1,972 testing scenes. The DL3DV-10K dataset is a large-scale collection featuring 10,510 scenes captured under controlled, standardized conditions.

**Implementation Details.** Our video generation model is based on SVD [3], an image-video diffusion model based on UNet. In our experiments, we use a relative camera system in which all camera poses are converted to poses relative to the first frame. The camera in the first frame is located at the world origin. In the first stage, we train the model at a resolution of  $320 \times 512$  for 50,000 iterations with the frame length set to 25. Subsequently, we train on  $576 \times 1024$  for 10,000 iterations to adapt to high resolution. The learning rate is set to  $1e - 5$  with a warmup of

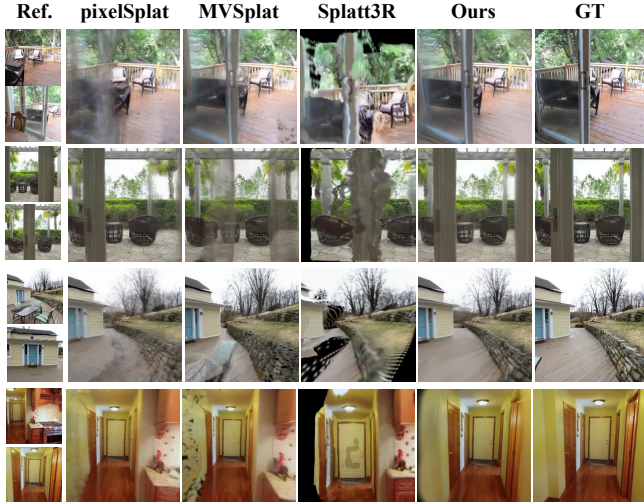


Figure 4. **Qualitative comparison** on Re10K [79]. Compared to baselines, we obtain superior reconstruction from limited overlap, and enhanced geometry reconstruction in non-overlapping regions.

Method	3-view			6-view			9-view		
	PSNR $\uparrow$	SSIM $\uparrow$	LPIPS $\downarrow$	PSNR $\uparrow$	SSIM $\uparrow$	LPIPS $\downarrow$	PSNR $\uparrow$	SSIM $\uparrow$	LPIPS $\downarrow$
<b>Mip-NeRF360</b>									
Zip-NeRF [2]	12.77	0.271	0.705	13.61	0.284	0.663	14.30	0.312	0.633
ReconFusion [61]	15.50	0.358	0.585	16.93	0.401	0.544	18.19	0.432	0.511
CAT3D [16]	16.62	0.377	0.515	17.72	0.425	0.482	18.67	0.460	0.460
ReconX [33]	17.16	0.435	0.407	19.20	0.473	0.378	20.13	0.482	0.356
ViewCrafter [71]	14.51	0.315	0.682	15.87	0.336	0.665	16.45	0.348	0.655
Ours	<b>17.32</b>	<b>0.439</b>	<b>0.418</b>	<b>19.42</b>	<b>0.510</b>	<b>0.371</b>	<b>20.19</b>	<b>0.536</b>	<b>0.345</b>
<b>DTU</b>									
Zip-NeRF [2]	9.18	0.601	0.383	8.84	0.589	0.370	9.23	0.592	0.364
FSGS [81]	17.34	0.818	0.169	21.55	0.880	0.127	24.33	0.911	0.106
ReconFusion [61]	20.74	0.875	0.124	23.62	<b>0.904</b>	0.105	24.62	0.921	0.094
CAT3D [16]	22.02	0.844	0.121	24.28	0.899	0.095	25.92	<b>0.928</b>	0.073
ViewCrafter [71]	15.63	0.522	0.383	15.03	0.525	0.408	14.92	0.487	0.452
Ours	<b>27.92</b>	<b>0.879</b>	<b>0.103</b>	<b>28.82</b>	0.895	<b>0.082</b>	<b>29.03</b>	0.905	<b>0.065</b>
<b>LLFF</b>									
Zip-NeRF [2]	17.23	0.574	0.373	20.71	0.764	0.221	23.63	0.830	0.166
FSGS [81]	20.31	0.652	0.288	24.20	0.811	0.173	25.32	0.856	0.136
ReconFusion [61]	21.34	0.724	0.203	24.25	0.815	0.152	25.21	0.848	0.134
CAT3D [16]	21.58	0.731	0.181	24.71	<b>0.833</b>	<b>0.121</b>	25.63	<b>0.860</b>	0.107
ViewCrafter [71]	17.73	0.521	0.332	17.43	0.512	0.345	17.33	0.488	0.351
Ours	<b>22.04</b>	<b>0.741</b>	<b>0.165</b>	<b>25.11</b>	0.814	0.124	<b>25.95</b>	0.838	<b>0.103</b>

Table 2. **Quantitative comparison** of sparse view 3D reconstruction on Out-of-Domain Datasets.

1,000 steps, using the Adam optimizer. We chose Lightning as the training framework, using mixed-precision fp16 and DeepSpeed ZeRO-2. We trained the proposed method and its variants on 16 NVIDIA A800 GPUs with a batch size of 32. During inference, we adopt DDIM sampler [49] with classifier-free guidance [21].

**Progressive Training.** Controlling a video generation model to generate arbitrary motion trajectories remains a challenging task. To enable robust arbitrary trajectory generation, we employ a three-stage curriculum learning strategy. The model first trains on smooth camera motions with small temporal intervals, then progressively adapts to more complex motion patterns through linear interval scheduling, and finally incorporates random sampling intervals. This gradual transition from simple to complex trajectories proves crucial for high-quality video generation with arbitrary trajectories.

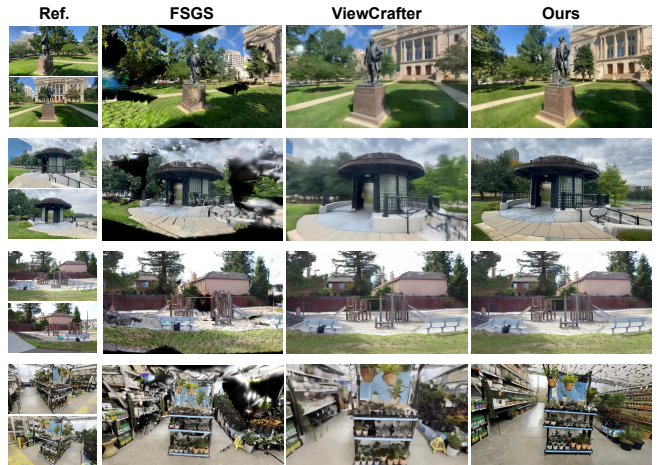


Figure 5. **Qualitative comparison** on DL3DV and Tank-and-Temples dataset. Our method reconstructs better than baselines, even with limited image overlap and in non-overlapping regions.

Method	RealEstate10K			ACID		
	PSNR $\uparrow$	SSIM $\uparrow$	LPIPS $\downarrow$	PSNR $\uparrow$	SSIM $\uparrow$	LPIPS $\downarrow$
pixelNeRF [69]	20.43	0.589	0.550	20.97	0.547	0.533
GPNR [50]	24.11	0.793	0.255	25.28	0.764	0.332
AttnRend [12]	24.78	0.820	0.213	26.88	0.799	0.218
MuRF [64]	26.10	0.858	0.143	28.09	0.841	0.155
pixelSplat [8]	25.89	0.858	0.142	28.14	0.839	0.150
MVSplat [9]	26.39	0.869	0.128	28.25	0.843	0.144
GS-LRM [73]	28.10	0.892	0.114	-	-	-
DepthSplat [65]	24.23	0.790	0.217	-	-	-
ReconX [33]	28.31	<b>0.912</b>	<b>0.088</b>	28.84	0.891	<b>0.101</b>
ViewCrafter [71]	24.22	0.788	0.218	23.48	0.660	0.299
Ours	<b>28.35</b>	0.862	0.121	<b>28.93</b>	<b>0.899</b>	0.116

Table 3. **Quantitative comparison** of two-view sparse view reconstruction methods on RealEstate10K [79] and ACID [32] dataset.

## 4.2. Comparisons

### 4.2.1. Controllable Video Generation

**Benchmark and Metrics.** We evaluate our video generation model against three baselines [20, 60, 71] on three benchmark datasets: RealEstate10K [79] (500 randomly selected videos with first frame as image condition and subsequent frames at stride 3 for pose guidance), DL3DV-140 [31] (500 video clips at stride 2), and Tanks-and-Temples [27] (100 sequences at stride 4 from 14 scenes with COLMAP-annotated poses) for out-of-domain generalization testing.

**Metrics.** Our evaluation framework employs multiple metrics to assess performance: visual quality measured through Fréchet Video Distance (FVD) and Fréchet Inception Distance (FID); camera control precision quantified by rotation error ( $R_{err}$ ) and translation error ( $T_{err}$ ) computed from camera poses extracted via COLMAP and normalized relative to the first frame; and visual consistency evaluated us-

Method	Small			Large		
	PSNR $\uparrow$	SSIM $\uparrow$	LPIPS $\downarrow$	PSNR $\uparrow$	SSIM $\uparrow$	LPIPS $\downarrow$
pixelNeRF [69]	18.417	0.601	0.526	20.869	0.639	0.458
AttnNeRF [12]	19.151	0.663	0.368	25.897	0.845	0.229
pixelSplat [8]	20.263	0.717	0.266	27.151	0.879	0.122
MVSplat [9]	20.353	0.724	0.254	27.408	0.884	0.116
DUS $\ddot{t}$ 3R [56]	14.101	0.432	0.468	16.427	0.453	0.402
CoPoNeRF [22]	17.393	0.585	0.462	20.464	0.652	0.358
<b>Ours</b>	<b>22.514</b>	<b>0.784</b>	<b>0.213</b>	<b>27.411</b>	<b>0.913</b>	<b>0.109</b>

Table 4. **Quantitative comparison** on the RealEstate10K dataset. *Small* and *Large* refer to input images with low and high overlap ratios, respectively. Greater overlap means greater temporal coherence between adjacent images.

ing PSNR, SSIM, and LPIPS [75] between generated and ground-truth views. To ensure fair comparison across methods with varying output capabilities, we restrict visual similarity assessment to the first 14 frames, as generated content typically diverges progressively from the conditional single-view input as the scene extends.

**Comparison.** Table 1 shows that our method excels in qualitative results, outperforming other methods in terms of visual quality, pose control, and 3D consistency. Figure 3 further demonstrates our advantage in 3D consistency and visual quality. This performance improvement is attributed to the introduction of a camera parameterization method and an epipolar attention module, which respectively enhance pose control ability and the 3D consistency of generated videos. In addition, training on a diverse scene dataset significantly improves the generalization ability of the model.

#### 4.2.2. Sparse View Reconstruction

**Benchmark and Metrics.** To comprehensively evaluate the performance of our method, we compare it with two categories of reconstruction methods: (1) two-view feed-forward reconstruction methods [8, 9, 12, 50, 65, 73], and (2) optimization-based sparse-view reconstruction methods [14, 16, 33, 71]. The evaluation employs two types of test sets: in-domain test sets (from RealEstate10K [79] and Acid [32]) and out-of-domain test sets. To ensure a fair comparison, the out-of-domain test set is the same as that used in previous work [16, 61]. For evaluating scene reconstruction quality, we adopt three metrics: PSNR, SSIM, and LPIPS [75]. Additionally, we categorize the evaluation into two groups based on the overlap between input views, with detailed overlap estimation methods provided in the supplementary materials. The evaluation protocol follows a consistent procedure: first, we reconstruct the 3D scene based on the input images, then render from novel views, and compute the metrics between the rendered images and the reference images.

**Comparison.** As shown in Tables 2-4 and Figures 4-5, our method performs well on various evaluation metrics, particularly in challenging scenarios with occlusions and limited view overlap. This improvement can be attributed to our



Figure 6. **Qualitative comparisons** of novel views rendered from scenes reconstructed using other 3D generation methods.

Dataset	Tanks-and-Temples			DL3DV		
	PSNR $\uparrow$	SSIM $\uparrow$	LPIPS $\downarrow$	PSNR $\uparrow$	SSIM $\uparrow$	LPIPS $\downarrow$
LucidDreamer [10]	14.552	0.364	0.415	15.126	0.452	0.431
ZeroNVS [43]	14.734	0.381	0.480	15.163	0.464	0.466
MotionCtrl [60]	15.322	0.426	0.404	16.889	0.528	0.392
ViewCrafter [71]	21.286	0.654	0.193	21.373	0.686	0.244
<b>Ours</b>	<b>22.331</b>	<b>0.742</b>	<b>0.213</b>	<b>22.782</b>	<b>0.791</b>	<b>0.202</b>

Table 5. **Quantitative comparison** of single-view novel view synthesis on DL3DV [31] and Tank-and-Temples [27] benchmarks.

approach that utilizes scene priors and sparse input views to generate helpful additional observations, thereby enhancing visual correlations between different viewpoints and helping to reduce the complexity of sparse-view reconstruction. Compared to the method [71] conditioning on point-based rendering, our approach shows advantages in reconstructing scenes with thin structures, leading to improved 3D reconstruction results.

#### 4.2.3. Single View 3D Generation

**Benchmark and Metrics.** In single-view generation, we compare our method with several generative methods [43, 44, 60, 71] on the Tank-and-Temples [27] and DL3DV-140 [31] datasets. Noted that we begin by reconstructing the 3D scene from the given images, followed by calculating the metrics using renderings from novel views. Similarly, we used the PSNR, SSIM, and LPIPS [75] metrics to evaluate our results. Evaluation in this underconstrained setting is challenging, as multiple 3D scenes can produce consistent generations for a given view. Thus, we measure metrics using only temporally adjacent frames to the conditional image, 14 sampled frames and poses captured after the conditional image.

**Comparison.** As shown in Table 5, our method consistently achieves superior performance on image quality metrics compared to the baselines. For a fair comparison with ZeroNVS [43] and LucidDreamer [10], which are limited

Method	$T_{err} \downarrow$	$R_{err} \downarrow$	COLMAP $_{err} \downarrow$	FVD $\downarrow$
Raw Value Emb.	1.592	2.376	13.5%	81.854
Quaternion Emb.	1.457	2.394	13.1%	80.368
W/o Ray Emb.	2.683	3.145	15.7%	112.843
W/o Epipolar	1.125	2.235	12.2%	79.547
W/o Scale Align.	1.712	2.498	14.3%	81.679
<b>Full model</b>	<b>1.014</b>	<b>2.218</b>	<b>4.2%</b>	<b>78.132</b>

Table 6. **Ablation study** on the video diffusion model variants.

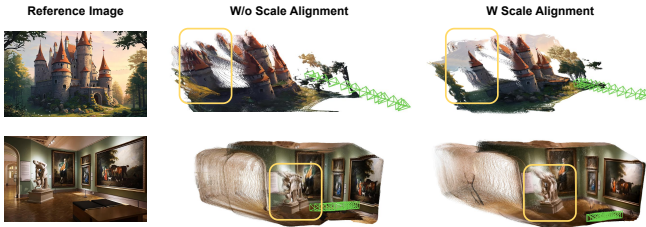


Figure 7. **Ablation on the scale alignment.** The video reconstruction results obtained based on scale-alignment training exhibit reduced artifacts while improving the 3D consistency of the scene.

to square image inputs, we crop the generated novel views before computing the quantitative metrics. Figure 6 shows that scenes reconstructed using our method have less noise and distortion in occluded areas.

### 4.3. Ablation Study

**Ablation on Video Diffusion Model.** We evaluate the effectiveness of the design choices. As shown in Table 6, ray embedding achieves significant improvements in camera control accuracy and rendering quality compared to other camera encoding methods by introducing denser position encoding and optimizing geometric correspondences. Specifically, cross-frame consistency shows notable enhancement. Furthermore, when incorporating geometric constraints through Epipolar Attention, the system achieves optimal performance in terms of camera controllability and 3D consistency.

**Scale Alignment.** As illustrated in Table 6 and Figure 7, the incorporation of dataset metric scale alignment significantly improves the pose control accuracy and 3D consistency of the generated video.

**Video Latent-based Reconstruction.** As demonstrated in Figure 8, incorporating generative priors and depth features in our method significantly enhances the fidelity of fine-grained geometric details in scene reconstruction. By introducing priors from video generative models, we reduced the difficulty of sparse-view reconstruction and achieved reasonable completion of unseen regions.

### 4.4. Discussions

Existing commercial video generation models like Kling and GEN-3 Turbo face a critical challenge: significant differences in input viewing angles often result in unnatural

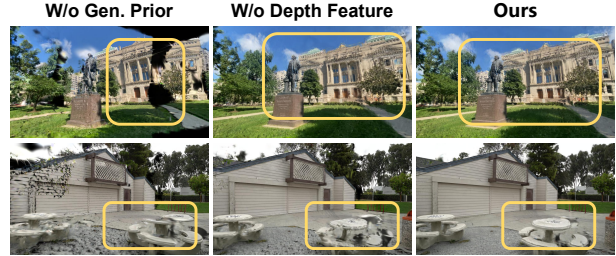


Figure 8. **Ablation on the feed-forward Reconstruction Module.**

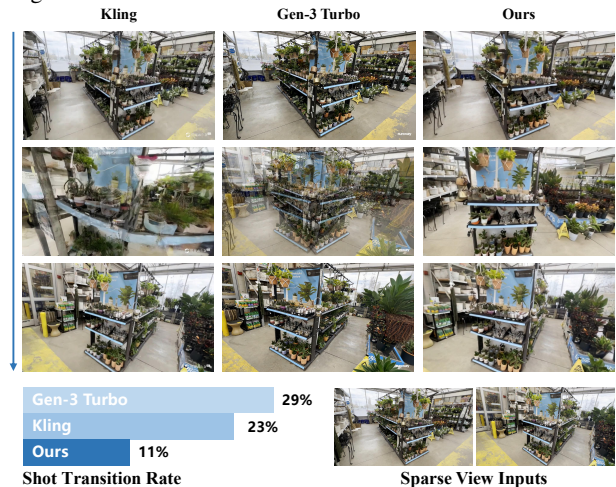


Figure 9. **Qualitative comparison** of video results. Our method outperforms other video generation models by reducing the shot transition rate and ensuring smooth transitions, particularly when faced with large differences in input viewing angles.

camera transitions. As shown in Figure 9, our approach effectively addresses this issue by fine-tuning the video generation model on extensive 3D scene datasets and integrating specific 3D information during the inference process. This enables our model to produce videos with more continuous and natural camera transitions.

## 5. Conclusion

We present *SpatialCrafter*, a framework for scene reconstruction and novel view synthesis from sparse or single-view inputs. By leveraging video diffusion models to generate plausible additional observations, we effectively reduce the complexity of sparse-view scene reconstruction. Our key contributions include: (1) precise camera control via ray embeddings or depth-warped images with a trainable condition encoder; (2) a unified scale estimator solving the scale ambiguity in multi-dataset training; and (3) a hybrid Mamba-Transformer architecture that combines monocular depth priors with semantic features from video latent space to directly regress 3D Gaussian primitives. Experiments show our method outperforms existing methods, especially in single-view extrapolation and scenarios with little overlaps. Future work will focus on handling extreme complex geometries, and extending to dynamic scene reconstruction.

## References

- [1] Sherwin Bahmani, Ivan Skorokhodov, Guocheng Qian, Aliaksandr Siarohin, Willi Menapace, Andrea Tagliasacchi, David B Lindell, and Sergey Tulyakov. Ac3d: Analyzing and improving 3d camera control in video diffusion transformers. *arXiv preprint arXiv:2411.18673*, 2024. 3
- [2] Jonathan T Barron, Ben Mildenhall, Dor Verbin, Pratul P Srinivasan, and Peter Hedman. Zip-nerf: Anti-aliased grid-based neural radiance fields. In *Proceedings of the IEEE/CVF International Conference on Computer Vision*, pages 19697–19705, 2023. 6
- [3] Andreas Blattmann, Tim Dockhorn, Sumith Kulal, Daniel Mendelevitch, Maciej Kilian, Dominik Lorenz, Yam Levi, Zion English, Vikram Voleti, Adam Letts, et al. Stable video diffusion: Scaling latent video diffusion models to large datasets. *arXiv preprint arXiv:2311.15127*, 2023. 5, 12
- [4] Andreas Blattmann, Tim Dockhorn, Sumith Kulal, Daniel Mendelevitch, Maciej Kilian, Dominik Lorenz, Yam Levi, Zion English, Vikram Voleti, Adam Letts, et al. Stable video diffusion: Scaling latent video diffusion models to large datasets. *arXiv preprint arXiv:2311.15127*, 2023. 4
- [5] Aleksei Bochkovskii, Amaël Delaunoy, Hugo Germain, Marcel Santos, Yichao Zhou, Stephan R Richter, and Vladlen Koltun. Depth pro: Sharp monocular metric depth in less than a second. *arXiv preprint arXiv:2410.02073*, 2024. 4
- [6] Chenjie Cao, Chaohui Yu, Shang Liu, Fan Wang, Xiangyang Xue, and Yanwei Fu. Mvgenmaster: Scaling multi-view generation from any image via 3d priors enhanced diffusion model. *arXiv preprint arXiv:2411.16157*, 2024. 3
- [7] Eric R Chan, Koki Nagano, Matthew A Chan, Alexander W Bergman, Jeong Joon Park, Axel Levy, Miika Aittala, Shalini De Mello, Tero Karras, and Gordon Wetzstein. Generative novel view synthesis with 3d-aware diffusion models. In *ICCV*, 2023. 3
- [8] David Charatan, Sizhe Lester Li, Andrea Tagliasacchi, and Vincent Sitzmann. pixelsplat: 3d gaussian splats from image pairs for scalable generalizable 3d reconstruction. In *CVPR*, 2024. 2, 6, 7, 12
- [9] Yuedong Chen, Haofei Xu, Chuanxia Zheng, Bohan Zhuang, Marc Pollefeys, Andreas Geiger, Tat-Jen Cham, and Jianfei Cai. Mvsplat: Efficient 3d gaussian splatting from sparse multi-view images. In *ECCV*, 2024. 2, 6, 7, 12
- [10] Jaeyoung Chung, Suyoung Lee, Hyeongjin Nam, Jaerin Lee, and Kyoung Mu Lee. Luciddreamer: Domain-free generation of 3d gaussian splatting scenes. *arXiv preprint arXiv:2311.13384*, 2023. 3, 7
- [11] Matt Deitke, Dustin Schwenk, Jordi Salvador, Luca Weihs, Oscar Michel, Eli VanderBilt, Ludwig Schmidt, Kiana Ehsani, Aniruddha Kembhavi, and Ali Farhadi. Objaverse: A universe of annotated 3d objects. In *CVPR*, 2023. 3
- [12] Yilun Du, Cameron Smith, Ayush Tewari, and Vincent Sitzmann. Learning to render novel views from wide-baseline stereo pairs. In *Proceedings of the IEEE/CVF Conference on Computer Vision and Pattern Recognition*, pages 4970–4980, 2023. 6, 7
- [13] Paul Engstler, Andrea Vedaldi, Iro Laina, and Christian Rupprecht. Invisible stitch: Generating smooth 3d scenes with depth inpainting. *arXiv preprint arXiv:2404.19758*, 2024. 3
- [14] Zhiwen Fan, Wenyan Cong, Kairun Wen, Kevin Wang, Jian Zhang, Xinghao Ding, Danfei Xu, Boris Ivanovic, Marco Pavone, Georgios Pavlakos, et al. Instantsplat: Unbounded sparse-view pose-free gaussian splatting in 40 seconds. *arXiv:2403.20309*, 2024. 2, 7, 12
- [15] Rafail Fridman, Amit Abecasis, Yoni Kasten, and Tali Dekel. Scenescape: Text-driven consistent scene generation. *Advances in Neural Information Processing Systems*, 36, 2024. 3
- [16] Riqi Gao, Aleksander Holynski, Philipp Henzler, Arthur Brussee, Ricardo Martin-Brualla, Pratul Srinivasan, Jonathan T Barron, and Ben Poole. Cat3d: Create anything in 3d with multi-view diffusion models. *arXiv preprint arXiv:2405.10314*, 2024. 3, 6, 7, 13
- [17] Albert Gu and Tri Dao. Mamba: Linear-time sequence modeling with selective state spaces. *arXiv preprint arXiv:2312.00752*, 2023. 5
- [18] Guangcong, Zhaoxi Chen, Chen Change Loy, and Ziwei Liu. Sparsenerf: Distilling depth ranking for few-shot novel view synthesis. In *ICCV*, 2023. 2
- [19] Yuwei Guo, Ceyuan Yang, Anyi Rao, Yaohui Wang, Yu Qiao, Dahua Lin, and Bo Dai. Animatediff: Animate your personalized text-to-image diffusion models without specific tuning. *arXiv preprint arXiv:2307.04725*, 2023. 3
- [20] Hao He, Yinghao Xu, Yuwei Guo, Gordon Wetzstein, Bo Dai, Hongsheng Li, and Ceyuan Yang. Cameractrl: Enabling camera control for text-to-video generation. *arXiv preprint arXiv:2404.02101*, 2024. 2, 3, 4, 5, 6
- [21] Jonathan Ho and Tim Salimans. Classifier-free diffusion guidance. *arXiv preprint arXiv:2207.12598*, 2022. 6, 12
- [22] Sunghwan Hong, Jaewoo Jung, Heeseong Shin, Jiaolong Yang, Seungryong Kim, and Chong Luo. Unifying correspondence pose and nerf for generalized pose-free novel view synthesis. In *Proceedings of the IEEE/CVF Conference on Computer Vision and Pattern Recognition*, pages 20196–20206, 2024. 2, 7
- [23] Yicong Hong, Kai Zhang, Jiuxiang Gu, Sai Bi, Yang Zhou, Difan Liu, Feng Liu, Kalyan Sunkavalli, Trung Bui, and Hao Tan. Lrm: Large reconstruction model for single image to 3d. In *ICLR*, 2024. 2
- [24] Li Hu. Animate anyone: Consistent and controllable image-to-video synthesis for character animation. In *Proceedings of the IEEE/CVF Conference on Computer Vision and Pattern Recognition*, pages 8153–8163, 2024. 3
- [25] Bernhard Kerbl, Georgios Kopanas, Thomas Leimkühler, and George Drettakis. 3d gaussian splatting for real-time radiance field rendering. *ACM TOG*, 2023. 2, 3
- [26] Mijeong Kim, Seonguk Seo, and Bohyung Han. Infonerf: Ray entropy minimization for few-shot neural volume rendering. In *CVPR*, 2022. 2
- [27] Arno Knapitsch, Jaesik Park, Qian-Yi Zhou, and Vladlen Koltun. Tanks and temples: Benchmarking large-scale scene reconstruction. *ACM Transactions on Graphics*, 36(4), 2017. 6, 7, 17

- [28] Vincent Leroy, Yohann Cabon, and Jérôme Revaud. Grounding image matching in 3d with mast3r. *arXiv preprint arXiv:2406.09756*, 2024. 2
- [29] Jiahe Li, Jiawei Zhang, Xiao Bai, Jin Zheng, Xin Ning, Jun Zhou, and Lin Gu. Dngaussian: Optimizing sparse-view 3d gaussian radiance fields with global-local depth normalization. In *CVPR*, 2024. 2, 12
- [30] Lingen Li, Zhaoyang Zhang, Yaowei Li, Jiale Xu, Xiaoyu Li, Wenbo Hu, Weihao Cheng, Jinwei Gu, Tianfan Xue, and Ying Shan. Nvcomposer: Boosting generative novel view synthesis with multiple sparse and unposed images. *arXiv preprint arXiv:2412.03517*, 2024. 2, 3
- [31] Lu Ling, Yichen Sheng, Zhi Tu, Wentian Zhao, Cheng Xin, Kun Wan, Lantao Yu, Qianyu Guo, Zixun Yu, Yawen Lu, et al. D13dv-10k: A large-scale scene dataset for deep learning-based 3d vision. In *CVPR*, 2024. 4, 5, 6, 7, 17
- [32] Andrew Liu, Richard Tucker, Varun Jampani, Ameesh Makadia, Noah Snavely, and Angjoo Kanazawa. Infinite nature: Perpetual view generation of natural scenes from a single image. In *Proceedings of the IEEE/CVF International Conference on Computer Vision*, pages 14458–14467, 2021. 5, 6, 7
- [33] Fangfu Liu, Wenqiang Sun, Hanyang Wang, Yikai Wang, Haowen Sun, Junliang Ye, Jun Zhang, and Yueqi Duan. Reconx: Reconstruct any scene from sparse views with video diffusion model. *arXiv preprint arXiv:2408.16767*, 2024. 2, 3, 6, 7, 13
- [34] Ruoshi Liu, Rundi Wu, Basile Van Hoorick, Pavel Tokmakov, Sergey Zakharov, and Carl Vondrick. Zero-1-to-3: Zero-shot one image to 3d object. In *Proceedings of the IEEE/CVF international conference on computer vision*, pages 9298–9309, 2023. 2, 3
- [35] Yuan Liu, Cheng Lin, Zijiao Zeng, Xiaoxiao Long, Lingjie Liu, Taku Komura, and Wenping Wang. Syncdreamer: Generating multiview-consistent images from a single-view image. *arXiv preprint arXiv:2309.03453*, 2023. 3
- [36] Baorui Ma, Huachen Gao, Haoge Deng, Zhengxiong Luo, Tiejun Huang, Lulu Tang, and Xinlong Wang. You see it, you got it: Learning 3d creation on pose-free videos at scale. *arXiv preprint arXiv:2412.06699*, 2024. 3
- [37] Norman Müller, Katja Schwarz, Barbara Rössle, Lorenzo Porzi, Samuel Rota Bulò, Matthias Nießner, and Peter Kotschieder. Multidiff: Consistent novel view synthesis from a single image. In *CVPR*, 2024. 3
- [38] Thomas Müller, Alex Evans, Christoph Schied, and Alexander Keller. Instant neural graphics primitives with a multiresolution hash encoding. *ACM Transactions on Graphics (ToG)*, 41(4):1–15, 2022. 2
- [39] Michael Niemeyer, Jonathan T Barron, Ben Mildenhall, Mehdi SM Sajjadi, Andreas Geiger, and Noha Radwan. Regnerf: Regularizing neural radiance fields for view synthesis from sparse inputs. In *CVPR*, 2022. 2
- [40] Ben Poole, Ajay Jain, Jonathan T Barron, and Ben Mildenhall. Dreamfusion: Text-to-3d using 2d diffusion. In *ICLR*, 2023. 3
- [41] Christian Reiser, Songyou Peng, Yiyi Liao, and Andreas Geiger. Kilonerf: Speeding up neural radiance fields with thousands of tiny mlps. In *ICCV*, 2021. 2
- [42] Robin Rombach, Andreas Blattmann, Dominik Lorenz, Patrick Esser, and Björn Ommer. High-resolution image synthesis with latent diffusion models. In *CVPR*, 2022. 3
- [43] Kyle Sargent, Zizhang Li, Tanmay Shah, Charles Herrmann, Hong-Xing Yu, Yunzhi Zhang, Eric Ryan Chan, Dmitry Lagun, Li Fei-Fei, Deqing Sun, and Jiajun Wu. ZeroNVS: Zero-shot 360-degree view synthesis from a single real image. In *CVPR*, 2024. 2, 3, 7
- [44] Junyoung Seo, Kazumi Fukuda, Takashi Shibuya, Takuya Narihira, Naoki Murata, Shoukang Hu, Chieh-Hsin Lai, Seungryong Kim, and Yuki Mitsufuji. Genwarp: Single image to novel views with semantic-preserving generative warping. *arXiv preprint arXiv:2405.17251*, 2024. 7
- [45] Yichun Shi, Peng Wang, Jianglong Ye, Mai Long, Kejie Li, and Xiao Yang. Mvdream: Multi-view diffusion for 3d generation. *arXiv preprint arXiv:2308.16512*, 2023. 3
- [46] Jaidev Shriram, Alex Trevithick, Lingjie Liu, and Ravi Ramamoorthi. Realdreamer: Text-driven 3d scene generation with inpainting and depth diffusion. *arXiv preprint arXiv:2404.07199*, 2024. 3
- [47] Vincent Sitzmann, Semon Rezchikov, Bill Freeman, Josh Tenenbaum, and Fredo Durand. Light field networks: Neural scene representations with single-evaluation rendering. *Advances in Neural Information Processing Systems*, 34: 19313–19325, 2021. 4
- [48] Brandon Smart, Chuanxia Zheng, Iro Laina, and Victor Adrian Prisacariu. Splatt3r: Zero-shot gaussian splatting from uncalibrated image pairs. *arXiv preprint arXiv:2408.13912*, 2024. 2
- [49] Jiaming Song, Chenlin Meng, and Stefano Ermon. Denoising diffusion implicit models. In *International Conference on Learning Representations*, 2020. 6, 12
- [50] Mohammed Suhail, Carlos Esteves, Leonid Sigal, and Ameesh Makadia. Generalizable patch-based neural rendering. In *European Conference on Computer Vision*, pages 156–174. Springer, 2022. 6, 7
- [51] Wenqiang Sun, Shuo Chen, Fangfu Liu, Zilong Chen, Yueqi Duan, Jun Zhang, and Yikai Wang. Dimensionx: Create any 3d and 4d scenes from a single image with controllable video diffusion. *arXiv preprint arXiv:2411.04928*, 2024. 3, 13
- [52] Stanislaw Szymanowicz, Eldar Insafutdinov, Chuanxia Zheng, Dylan Campbell, João F Henriques, Christian Rupprecht, and Andrea Vedaldi. Flash3d: Feed-forward generalisable 3d scene reconstruction from a single image. *arXiv preprint arXiv:2406.04343*, 2024. 2
- [53] Stanislaw Szymanowicz, Christian Rupprecht, and Andrea Vedaldi. Splatter image: Ultra-fast single-view 3d reconstruction. In *The IEEE/CVF Conference on Computer Vision and Pattern Recognition (CVPR)*, 2024. 2
- [54] Joseph Tung, Gene Chou, Ruojin Cai, Guandao Yang, Kai Zhang, Gordon Wetzstein, Bharath Hariharan, and Noah Snavely. Megascenes: Scene-level view synthesis at scale. *arXiv preprint arXiv:2406.11819*, 2024. 3
- [55] Ruicheng Wang, Sicheng Xu, Cassie Dai, Jianfeng Xiang, Yu Deng, Xin Tong, and Jiaolong Yang. Moge: Unlocking accurate monocular geometry estimation for open-domain images with optimal training supervision, 2024. 4

- [56] Shuzhe Wang, Vincent Leroy, Yohann Cabon, Boris Chidlovskii, and Jerome Revaud. Dust3r: Geometric 3d vision made easy. In *CVPR*, 2024. 2, 7
- [57] Xiang Wang, Hangjie Yuan, Shiwei Zhang, Dayou Chen, Jiniu Wang, Yingya Zhang, Yujun Shen, Deli Zhao, and Jingren Zhou. Videocomposer: Compositional video synthesis with motion controllability. *Advances in Neural Information Processing Systems*, 36, 2024. 3
- [58] Zirui Wang, Shangzhe Wu, Weidi Xie, Min Chen, and Victor Adrian Prisacariu. Nerf-: Neural radiance fields without known camera parameters. *arXiv preprint arXiv:2102.07064*, 2021. 2, 3
- [59] Zhengyi Wang, Cheng Lu, Yikai Wang, Fan Bao, Chongxuan Li, Hang Su, and Jun Zhu. Prolificdreamer: High-fidelity and diverse text-to-3d generation with variational score distillation. *Advances in Neural Information Processing Systems*, 36, 2024. 3
- [60] Zhouxia Wang, Ziyang Yuan, Xintao Wang, Tianshui Chen, Menghan Xia, Ping Luo, and Ying Shan. Motionctrl: A unified and flexible motion controller for video generation. In *SIGGRAPH Conference*, 2024. 2, 3, 4, 5, 6, 7
- [61] Rundi Wu, Ben Mildenhall, Philipp Henzler, Keunhong Park, Ruiqi Gao, Daniel Watson, Pratul P Srinivasan, Dor Verbin, Jonathan T Barron, Ben Poole, et al. Reconfusion: 3d reconstruction with diffusion priors. In *CVPR*, 2024. 2, 3, 6, 7
- [62] Yuanbo Xiangli, Linning Xu, Xingang Pan, Nanxuan Zhao, Anyi Rao, Christian Theobalt, Bo Dai, and Dahua Lin. Bungeenerf: Progressive neural radiance field for extreme multi-scale scene rendering. In *ECCV*, 2022. 2
- [63] Dejjia Xu, Weili Nie, Chao Liu, Sifei Liu, Jan Kautz, Zhangyang Wang, and Arash Vahdat. Camco: Camera-controllable 3d-consistent image-to-video generation. *arXiv preprint arXiv:2406.02509*, 2024. 3
- [64] Haofei Xu, Anpei Chen, Yuedong Chen, Christos Sakaridis, Yulun Zhang, Marc Pollefeys, Andreas Geiger, and Fisher Yu. Murf: Multi-baseline radiance fields. In *Proceedings of the IEEE/CVF Conference on Computer Vision and Pattern Recognition*, pages 20041–20050, 2024. 6
- [65] Haofei Xu, Songyou Peng, Fangjinhua Wang, Hermann Blum, Daniel Barath, Andreas Geiger, and Marc Pollefeys. Depthspat: Connecting gaussian splatting and depth. *arXiv preprint arXiv:2410.13862*, 2024. 2, 6, 7
- [66] Zhongcong Xu, Jianfeng Zhang, Jun Hao Liew, Hanshu Yan, Jia-Wei Liu, Chenxu Zhang, Jiashi Feng, and Mike Zheng Shou. Magicanimate: Temporally consistent human image animation using diffusion model. In *Proceedings of the IEEE/CVF Conference on Computer Vision and Pattern Recognition*, pages 1481–1490, 2024. 3
- [67] Jiawei Yang, Marco Pavone, and Yue Wang. Freenerf: Improving few-shot neural rendering with free frequency regularization. In *Proceedings of the IEEE/CVF conference on computer vision and pattern recognition*, pages 8254–8263, 2023. 2
- [68] Botao Ye, Sifei Liu, Haofei Xu, Xueting Li, Marc Pollefeys, Ming-Hsuan Yang, and Songyou Peng. No pose, no problem: Surprisingly simple 3d gaussian splats from sparse unposed images. *arXiv preprint arXiv:2410.24207*, 2024. 2
- [69] Alex Yu, Vickie Ye, Matthew Tancik, and Angjoo Kanazawa. pixelnerf: Neural radiance fields from one or few images. In *Proceedings of the IEEE/CVF Conference on Computer Vision and Pattern Recognition*, pages 4578–4587, 2021. 6, 7
- [70] Hong-Xing Yu, Haoyi Duan, Junhwa Hur, Kyle Sargent, Michael Rubinstein, William T Freeman, Forrester Cole, Deqing Sun, Noah Snavely, Jiajun Wu, et al. Wonderjourney: Going from anywhere to everywhere. In *Proceedings of the IEEE/CVF Conference on Computer Vision and Pattern Recognition*, pages 6658–6667, 2024. 3
- [71] Wangbo Yu, Jinbo Xing, Li Yuan, Wenbo Hu, Xiaoyu Li, Zhipeng Huang, Xiangjun Gao, Tien-Tsin Wong, Ying Shan, and Yonghong Tian. Viewcrafter: Taming video diffusion models for high-fidelity novel view synthesis. *arXiv preprint arXiv:2409.02048*, 2024. 3, 4, 5, 6, 7, 12
- [72] Jason Y Zhang, Amy Lin, Moneish Kumar, Tzu-Hsuan Yang, Deva Ramanan, and Shubham Tulsiani. Cameras as rays: Pose estimation via ray diffusion. In *International Conference on Learning Representations (ICLR)*, 2024. 4
- [73] Kai Zhang, Sai Bi, Hao Tan, Yuanbo Xiangli, Nanxuan Zhao, Kalyan Sunkavalli, and Zexiang Xu. Gs-irm: Large reconstruction model for 3d gaussian splatting. In *European Conference on Computer Vision*, pages 1–19. Springer, 2025. 2, 6, 7
- [74] Kai Zhang, Sai Bi, Hao Tan, Yuanbo Xiangli, Nanxuan Zhao, Kalyan Sunkavalli, and Zexiang Xu. Gs-irm: Large reconstruction model for 3d gaussian splatting. In *European Conference on Computer Vision*, pages 1–19. Springer, 2025. 2
- [75] Richard Zhang, Phillip Isola, Alexei A Efros, Eli Shechtman, and Oliver Wang. The unreasonable effectiveness of deep features as a perceptual metric. In *Proceedings of the IEEE conference on computer vision and pattern recognition*, pages 586–595, 2018. 7
- [76] Songchun Zhang, Yibo Zhang, Quan Zheng, Rui Ma, Wei Hua, Hujun Bao, Weiwei Xu, and Changqing Zou. 3d-scenedreamer: Text-driven 3d-consistent scene generation. In *Proceedings of the IEEE/CVF Conference on Computer Vision and Pattern Recognition*, pages 10170–10180, 2024. 3
- [77] Xiaoshuai Zhang, Sai Bi, Kalyan Sunkavalli, Hao Su, and Zexiang Xu. Nerfusion: Fusing radiance fields for large-scale scene reconstruction. In *CVPR*, 2022. 2
- [78] Chuanxia Zheng and Andrea Vedaldi. Free3d: Consistent novel view synthesis without 3d representation. In *Proceedings of the IEEE/CVF Conference on Computer Vision and Pattern Recognition*, pages 9720–9731, 2024. 3
- [79] Tinghui Zhou, Richard Tucker, John Flynn, Graham Fyffe, and Noah Snavely. Stereo magnification: Learning view synthesis using multiplane images. *ACM Trans. Graph*, 37, 2018. 4, 5, 6, 7
- [80] Tinghui Zhou, Richard Tucker, John Flynn, Graham Fyffe, and Noah Snavely. Stereo magnification: Learning view synthesis using multiplane images. *ACM TOG*, 2018. 3
- [81] Zehao Zhu, Zhiwen Fan, Yifan Jiang, and Zhangyang Wang. Fsgs: Real-time few-shot view synthesis using gaussian splatting. In *ECCV*, 2024. 2, 6

# Appendix

<b>A Implementation Details</b>	<b>12</b>
A.1 Training Details . . . . .	12
A.2 Evaluation Details . . . . .	12
<b>B Discussions</b>	<b>12</b>
B.1 Comparison with Very Recent Methods . . .	12
<b>C More Qualitative Results</b>	<b>13</b>
C.1 More Generated Video Results . . . . .	13
C.2 Basic Camera Trajectories . . . . .	13
C.3 Single View Exploration Results . . . . .	13
C.4 More 3D Reconstruction Results . . . . .	13
<b>D Limitations</b>	<b>13</b>

## A. Implementation Details

### A.1. Training Details

Our video generation model is built upon SVD [3], an image-video diffusion model based on UNet. The training process incorporates a continuous-time noise scheduler (Karras et al., 2022), enabling the model to learn to gradually denoise high-variance Gaussian noise. Specifically, we define the noisy data as  $x_t = x_0 + n(t)$ , where the added Gaussian noise  $n(t) \sim \mathcal{N}(0, \sigma^2(t)I)$ . The iterative denoising process corresponds to the probability flow ODE:

$$dx = -\dot{\sigma}(t)\sigma(t)\nabla_x \log p(x; \sigma(t))dt,$$

where  $\nabla_x \log p(x; \sigma(t))$  is the score function parameterized by a neural network  $D_\theta$ . The training objective focuses on denoising score matching:  $E[\|D_\theta(x_0 + n; \sigma, c) - x_0\|_2^2]$ , with  $c$  representing the conditioning information. We follow the EDM framework, parameterizing the learnable denoiser as  $D_\theta(x; \sigma) = c_{\text{skip}}(\sigma)x + c_{\text{out}}(\sigma)F_\theta(c_{\text{in}}(\sigma)x; c_{\text{noise}}(\sigma))$ .

In our work, we use a relative camera system to convert all camera poses relative to the first frame located at the world origin. First, we train the model at a resolution of  $320 \times 512$  with a frame length of 25, for 50,000 iterations, and we perform center cropping on the input images to standardize the resolution. Subsequently, we adjust the model to a higher resolution of  $576 \times 1024$  and continue training for another 10,000 iterations, setting the learning rate to  $1e-5$  and using the Adam optimizer with a 1,000-step warm-up. The training is conducted on 8 NVIDIA A800 GPUs with a batch size of 16. It is important to note that we only train the camera encoder, epipolar attention modules, and temporal attention while keeping the weights of other parts frozen. We first train on the Re10K and ACID datasets, with the sampling interval of video frames linearly increasing from 2 to 10. After that, we incorporate the DL3DV dataset, randomly sampling the video frame intervals between [2, 10]

to enable the model to adapt to different motion speeds. We choose Lightning as the training framework, utilizing mixed precision fp16 and DeepSpeed ZeRO-2 to enhance efficiency. During inference, we implement the DDIM sampler [49] alongside classifier-free guidance [21] to enhance performance.

### A.2. Evaluation Details

**Video Generation.** When using COLMAP to extract the camera pose of the generated video, the reliability of the obtained pose is often low. Therefore, we employ DUST3R for a more robust pose estimation. To compare with previous methods, we transform the camera coordinates of the estimated poses to be relative to the first frame and normalize the scale using the furthest frame. We then calculate the rotation distance relative to the ground truth rotation matrices of each generated novel view sequence, expressed as  $R_{\text{dist}} = \sum_{i=1}^n \arccos\left(\frac{\text{tr}(R_{\text{gen}}^i R_{\text{gt}}^{i^T}) - 1}{2}\right)$ . We also compute the  $T_{\text{dist}} = \sum_{i=1}^n \|T_{\text{gt}}^i - T_{\text{gen}}^i\|_2$ , which measures the Euclidean distance between ground truth and estimated translations across  $n$  video frames.

**Sparse View Reconstruction.** To ensure a fair comparison with feed-forward baselines [8, 9], we conducted experiments on  $256 \times 256$  resolutions. To comprehensively evaluate our method, we compared the results of input views under small and large overlap ratios. We employed RoMa to determine the overlap ratio of image pairs. First, we obtained dense matches from the first image to the second and vice versa, considering pixels with matching scores exceeding 0.005 as valid. Next, we calculated the overlap ratio for each image pair by dividing the number of valid matched pixels by the total number of pixels, with the final overlap ratio defined as the minimum of the two directional calculations. Additionally, to compare with optimization-based reconstruction baselines [14, 29], we used only 2 ground truth training images per scene and evaluated using 12 views. The evaluation metrics included PSNR, SSIM, and LPIPS.

## B. Discussions

### B.1. Comparison with Very Recent Methods

**ViewCrafter.** ViewCrafter [71] leverages point cloud rendering as a condition for fine-tuning video diffusion models. However, constrained by Dust3R’s capabilities, the approach may encounter challenges in synthesizing novel views with extensive view range transformations, particularly when generating front-view images from limited back-view inputs. Moreover, in scenarios where DUST3R fails—such as incorrectly predicting planar geometries—ViewCrafter’s performance can be significantly compromised. In contrast, our proposed generation module decouples from the reconstruction module, effectively

mitigating these limitations and enhancing view synthesis robustness.

**DimensionX.** DimensionX [51] achieves promising results by fine-tuning respective LORA models for different motion patterns. However, this method has some limitations: first, it cannot generate more complex motion patterns; second, it lacks effective control over the speed and amplitude of motion. In contrast, our method introduces camera embedding as the conditional signal, which effectively solves the above problems, thereby enabling the generation of more complex motion patterns and providing precise control over the speed and amplitude of motion.

**ReconX.** ReconX [33] initially constructs a global point cloud representation and encodes it into a contextual space, serving as 3D geometric conditional information for video diffusion models. However, the method’s performance critically depends on the geometric reconstruction accuracy of the underlying DUST3R algorithm. When DUST3R fails to precisely align and reconstruct geometric structures, the point cloud information injected into the video diffusion model may introduce significant geometric distortions, leading to suboptimal generation results. More importantly, the current approach is limited to multi-view interpolation scenarios, lacking an effective solution for single-view extrapolation tasks

**CAT3D.** CAT3D [16] extends the text-to-image (T2I) generation model by a large-scale data-driven method to learn a 3D prior of the scene, which usually requires a large amount of training time. In addition, the generation stage requires rendering a large number of frames (about 100 frames) to reconstruct the scene. We recognize that video generation models trained on large video datasets embed inherent scene prior information, and therefore propose a new method based on fine-tuning with a video diffusion model. Our method speeds up convergence and retains the generative prior of the pre-trained video model, thereby enhancing the model’s generalization ability. By introducing explicit geometric constraints, we further improve the 3D consistency of the generated scenes. Notably, during the inference stage, we utilize the geometric prior for initialization and reconstruction, greatly reducing the number of images required and the optimization time.

## C. More Qualitative Results

### C.1. More Generated Video Results

As shown in Figure 14, we present a series of generated video sequences covering different scenarios, including indoor environments, outdoor landscapes, and object-centered scenes. Our method shows excellent stability in generating video frame sequences with high 3D consistency, and can effectively predict the plausible appearance details of previously unseen regions. In addition, Figure 12

demonstrates the view interpolation ability of our video generation model using sparse input views, and the performance remains stable even when the input view angles differ greatly.

### C.2. Basic Camera Trajectories

Our method demonstrates promising generalization ability in camera-controllable video generation, especially for common motion patterns such as zoom-in, zoom-out, and panning. As shown in Figure 10, our method can generate stable videos with basic camera trajectories using a large-scale training dataset that contains a diverse and complex distribution of camera motion patterns. In addition, in Figure 11, we also show the control ability of our method for different motion amplitudes.

### C.3. Single View Exploration Results

Figure 13 illustrates that scene reconstruction from sparse input views often suffers from severe occlusions and geometric gaps due to limited observation angles. By implementing a multi-view observation strategy using video diffusion models, we can progressively fill in these missing regions, thereby enhancing the reconstruction’s completeness and geometric detail. As we continuously increase and synthesize observation perspectives, the scene’s geometric structure becomes more complete, significantly improving the quality and accuracy of the 3D reconstruction. In Figure 11, we show that by controlling the camera parameters, we can directly control the magnitude of the movement, which is general in different scenarios.

### C.4. More 3D Reconstruction Results

Figure 16 presents additional reconstruction and rendering results based on generated video frames, demonstrating that our method effectively achieves high-quality reconstructions in indoor, outdoor, and object-centered scenes.

## D. Limitations

Our method encounters several challenges in video generation and scene reconstruction. First, existing video diffusion models suffer from significant inference efficiency bottlenecks, particularly when processing large-scale scene reconstruction tasks requiring numerous video frames, leading to prohibitively high computational costs. Second, current video diffusion models are constrained in the number of generated video frames, which impedes comprehensive scene reconstruction for complex scenarios. Lastly, the lack of effective user interaction mechanisms represents a substantial limitation, as users cannot exert fine-grained control over the generation process and results, restricting the model’s adaptability in practical applications.

**Move Right**



**Move Left**



**Roll**



**Zoom in**



**Zoom out**



**Move Up**



Figure 10. Visualization of our method for generating videos with basic motion trajectories.



Figure 11. Visualization of our method for controlling different motion amplitudes.

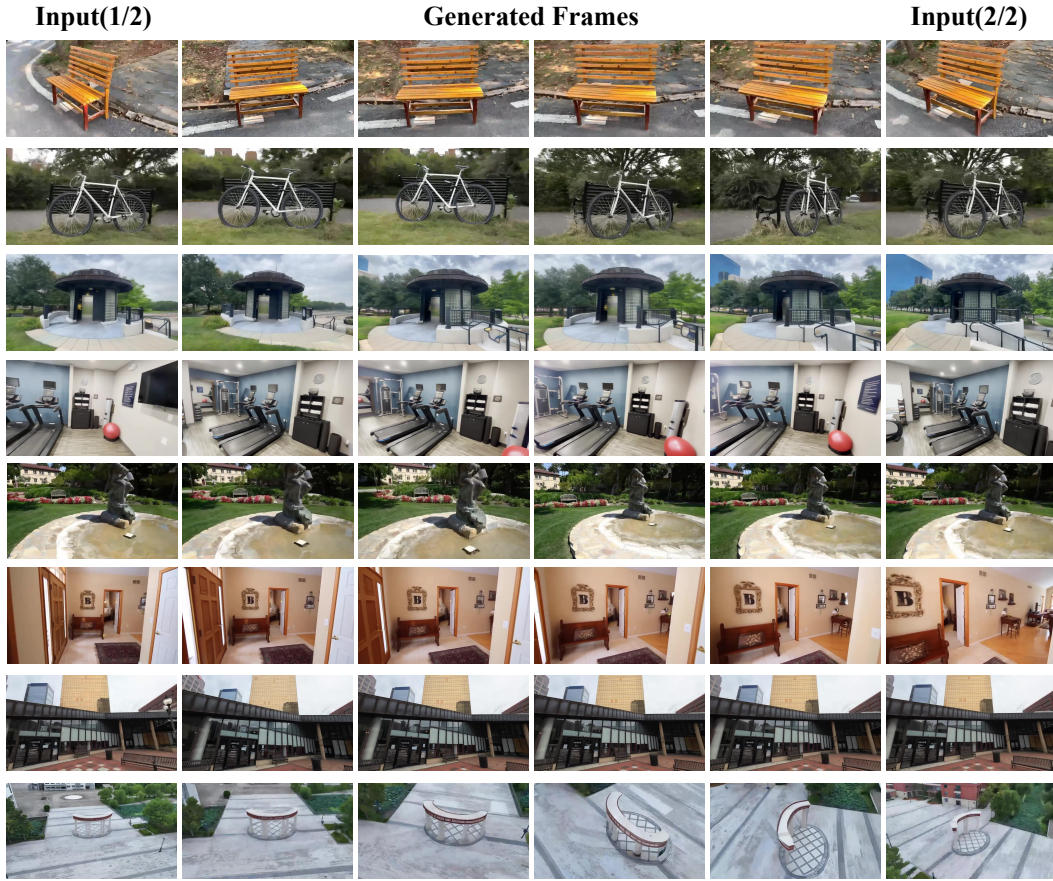


Figure 12. More Visualization of interpolated video based on sparse view input.

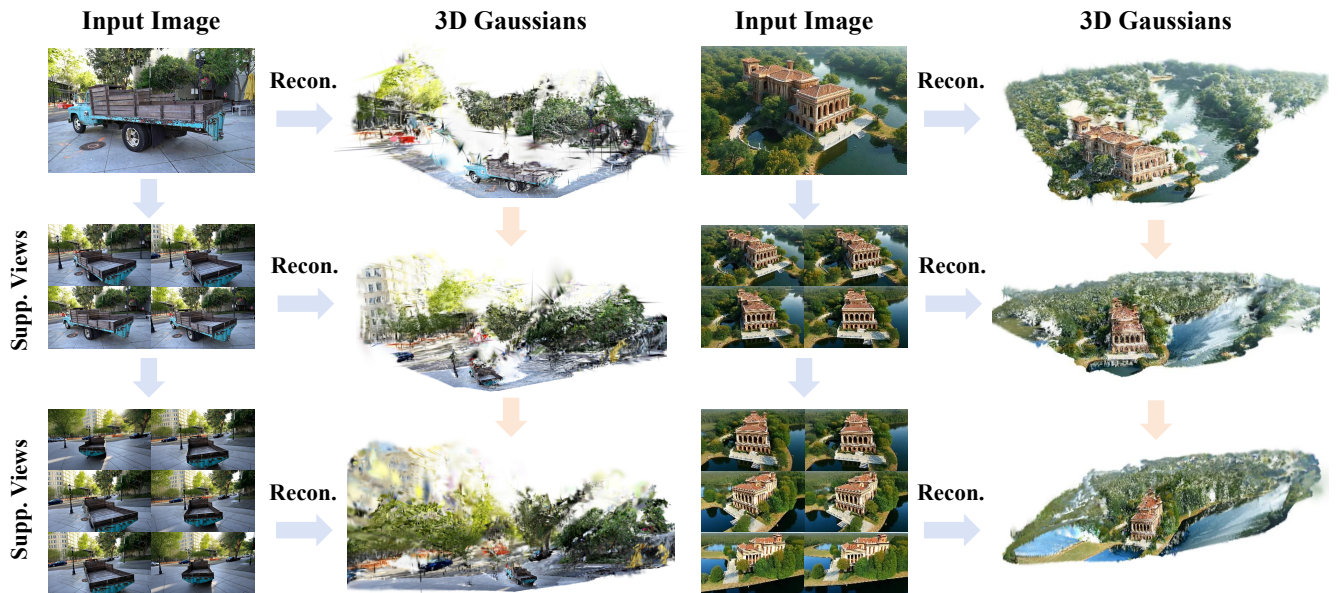


Figure 13. Visualization of exploration and reconstruction based on single-view input.



Figure 14. More video generation results with high 3D consistency based on single-view input.



Figure 15. **Consistent frames generated by our approach.** Our method demonstrates strong generalization capability across diverse scenarios, including the DL3DV [31], Tanks-and-Temples benchmark [27], and synthetic images from generative models, while maintaining geometric coherence and structural fidelity.

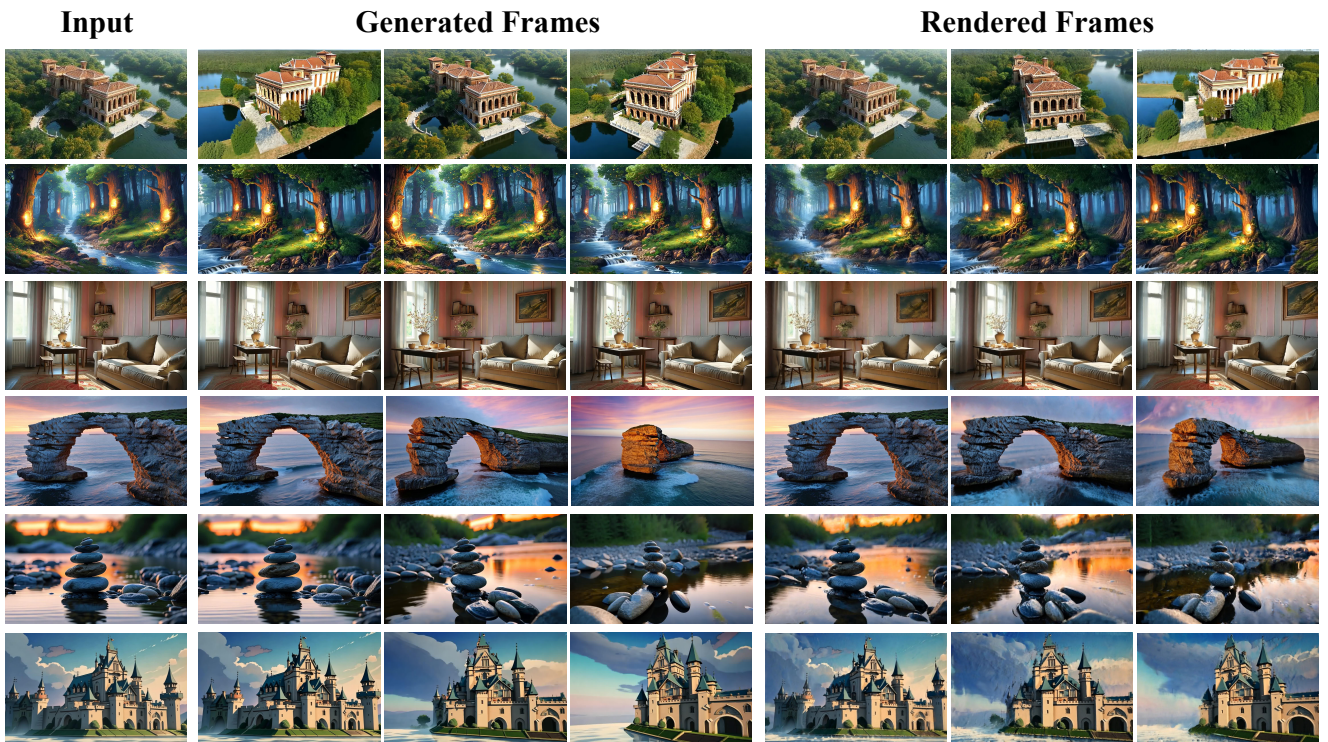


Figure 16. More video generation and reconstruction results with high 3D consistency based on single-view input.